AGU Advances

RESEARCH ARTICLE
10.1029/2023AV001134

Fault Orientation Trumps Fault Maturity in Controlling Coseismic Rupture Characteristics of the 2021 Maduo Earthquake

Jing Liu-Zeng[1], **Zhijun Liu**[1], **Xiaoli Liu**[2], **Chris Milliner**[3], **Alba M. Rodriguez Padilla**[3,4], **Shiqing Xu**[5], **Jean-Philippe Avouac**[3], **Wenqian Yao**[1], **Yann Klinger**[6], **Longfei Han**[1], **Yanxiu Shao**[1], **Xiaodong Yan**[1], **Saif Aati**[3], and **Zhigang Shao**[7]

[1]School of Earth System Science, Institute of Surface-Earth System Science, Tianjin University, Tianjin, China, [2]Key Laboratory of Earthquake Geodesy, Institute of Seismology, China Earthquake Administration, Wuhan, China, [3]Division of Geological and Planetary Sciences, California Institute of Technology, Pasadena, CA, USA, [4]Department of Earth and Planetary Sciences, University of California, Davis, CA, USA, [5]Department of Earth and Space Sciences, Southern University of Science and Technology, Shenzhen, China, [6]Institut de physique du globe de Paris, Paris, France, [7]China Earthquake Administration, Institute of Earthquake Prediction, Beijing, China

Peer Review The peer review history for this article is available as a PDF in the Supporting Information.

Key Points:

- The 2021 Mw 7.4 Maduo earthquake ruptured the east-growing tip zone of the slow-moving (~1 mm/yr) immature Jiangcuo fault in north Tibet
- Comparatively newly formed, optimally oriented segments accommodate more localized strain than structurally inherited misoriented segments
- Fault orientation with respect to the regional stress can exert a more important control than fault maturity on coseismic rupture behavior

Supporting Information:

Supporting Information may be found in the online version of this article.

Correspondence to:

J. Liu-Zeng,
liu_zeng@tju.edu.cn

Citation:

Liu-Zeng, J., Liu, Z., Liu, X., Milliner, C., Rodriguez Padilla, A. M., Xu, S., et al. (2024). Fault orientation trumps fault maturity in controlling coseismic rupture characteristics of the 2021 Maduo earthquake. *AGU Advances*, *5*, e2023AV001134. https://doi.org/10.1029/2023AV001134

Received 26 NOV 2023
Accepted 22 FEB 2024

Author Contributions:

Formal analysis: Saif Aati, Zhigang Shao
Investigation: Zhijun Liu, Xiaoli Liu, Wenqian Yao, Longfei Han, Yanxiu Shao, Xiaodong Yan
Writing – original draft: Jing Liu-Zeng
Writing – review & editing: Chris Milliner, Alba M. Rodriguez Padilla, Shiqing Xu, Jean-Philippe Avouac, Yann Klinger

Abstract

Fault maturity has been proposed to exert a first order control on earthquake rupture, yet direct observations linking individual rupture to long-term fault growth are rare. The 2021 Mw 7.4 Maduo earthquake ruptured the east-growing end of the slow-moving (~1 mm/yr) Jiangcuo fault in north Tibet, providing an opportunity to examine the relation between rupture characteristics and fault structure. Here we combine field and multiple remote sensing techniques to map the surface rupture at cm-resolution and document comprehensively on-fault offsets and off-fault deformation. The 158 km-long surface rupture consists of misoriented structurally inherited N110°-striking segments and younger optimally oriented N093°-striking segments, relative to the regional stress field. Despite being comparatively newly formed, the ~N093°-striking fault segments accommodate more localized strain, with up to 3 m on-fault left-lateral slip and 25%–50% off-fault deformation, and possibly faster rupture speed. These results are in contrast with previous findings showing more localized strain and faster rupture speed on more mature fault segments; instead, our observations suggest that fault orientation with respect to the regional stress can exert a more important control than fault maturity on coseismic rupture behavior when both factors are at play.

Plain Language Summary

One of the frontiers in earthquake science is to understand the complexity of earthquake rupture and the controlling factors. Probing the effect of fault maturity, among various structural and rheologic properties, has gained increasingly popularity in recent years. Yet direct observations linking individual earthquake ruptures to long-term fault growth are rare, rendering the seismological consequence of fault maturity often speculative. The 22 May 2021 Maduo earthquake, occurring in the east-growing end of the immature Jiangcuo fault (slip rate ~1 mm/yr and cumulative slip <5 km) in north Tibet, provides an excellent opportunity to tease apart the effect of fault structural and geometric properties on rupture behavior. We combine field and multiple remote sensing techniques to map the surface rupture of the Maduo earthquake at cm-resolution and to document comprehensively on-fault offsets and off-fault deformation. The Maduo rupture propagated on misoriented structurally inherited segments, linked by more optimally oriented segments, relative to regional principal stress. Strain is more localized on the comparatively newly formed and optimally oriented segments. In contrast to previous findings highlighting the role of fault maturity, our new observations suggest that the orientation with respect to the regional stress exerts a more important control on rupture dynamics.

1. Introduction

A strike-slip fault system evolves over time through growing in length, accumulating slip, and simplifying structurally. This evolution is observed in analog and numerical models (e.g., Du & Aydin, 1995; Naylor et al., 1986; Tchalenko, 1970), and might be inferred from fossil fault networks in bedrock outcrop or hydrocarbon explorations (Sylvester, 1988; Wilcox et al., 1973), and large-scale tectonics (Armijo et al., 1999). Fault growth is achieved through repeated earthquake ruptures and, possibly also aseismic slip (e.g., Cowie & Scholz, 1992; Manighetti et al., 2001; Mitchell & Faulkner, 2009; Perrin, Manighetti, & Gaudemer, 2016). The process affects the fault organization at all scales and might influence the source properties of earthquakes. For example, it has been proposed that immature faults, compared to more mature faults, often have a more complex geometry (Manighetti et al., 2021; Stirling et al., 1996; Wesnousky, 1988), produce slower rupture speed and smaller coseismic slip (Guo et al., 2023; Perrin, Manighetti, Ampuero, et al., 2016), higher percentage of off-fault deformation (Dolan & Haravitch, 2014; Milliner et al., 2021), and a wider deformation zone (Perrin et al., 2021). However, evolving faults intrinsically have spatially varying maturity and geologic inheritance along strike, for instance with more immature sections toward the fault propagation direction (Perrin, Manighetti, & Gaudemer, 2016).

Observations linking individual earthquake ruptures to long-term fault growth are rare, rendering the seismological consequence of fault maturity often speculative. For instance, empirical relations between rupture characteristics and fault structure are often hinged on the inference of long-term fault development or fault maturity (Manighetti et al., 2007, 2021; Perrin, Manighetti, Ampuero, et al., 2016; Stirling et al., 1996; Wesnousky, 1988). On the other hand, individual earthquake rupture, which broke a certain length of the pre-existing fault system, must carry the imprint of the geologic past and at the same time manifest itself as a snapshot of fault development in action. They can depart locally from more mature faults or fault segments (Ron et al., 2001). They can reactivate complex fault systems with a mix of optimally oriented and misoriented faults (Fletcher et al., 2016) and sometimes nearly orthogonal faults (Hudnut et al., 1989). Thus, understanding the link between earthquake rupture behavior and the geologic inheritance of faults can provide insights into fault growth and help inform seismic hazard assessment.

The 2021 *Mw* 7.4 Maduo strike-slip earthquake provides an excellent opportunity to test how fault growth occurs, overprinting pre-existing geologic fabrics, and how this process influences rupture dynamics. The rupture propagated bilaterally on the poorly known ∼1 mm/yr left-lateral Jiangcuo fault system (Cheng et al., 2023; Wei et al., 2022; Yue et al., 2022; Zhu et al., 2021), which is one of the secondary faults splaying south off the Kunlun fault and cutting diagonally across the Songpan-Garze terrane (Tapponnier et al., 2001) (Figure 1). These active subordinate faults developed upon a series of geologically mapped NW to NWW-striking faults, pre-existing structures inherited from prior phases of deformation (Figures 1c and 2). The surface rupture coincides mostly with geologically inherited fault segments in the west but cuts across them in the east (Qinghai Institute of Geological Survey, 2010) (Figure 2), allowing to evaluate the effect of along-strike structural differences on coseismic rupture characteristics.

In this study, we investigate in detail the distribution of surface ruptures, surface coseismic slip, and off-fault deformation from the Maduo earthquake. Through field investigation and Unmanned Aerial Vehicle (UAV) photogrammetry-based mapping, we produced a complete high-resolution map of coseismic fractures and over eight hundred offset measurements across discrete faults. UAV photogrammetry provides cm-resolution images covering the entire surface rupture for the first time for a large earthquake in Tibet. This facilitates detailed and exhaustive mapping of fractures that would be inaccessible in the field due to the high elevation (>4,200 m a.s.l.) and harsh environment. We combine our rupture maps with the surface deformation field obtained from the correlation of pre- and post-earthquake satellite images to evaluate the off-fault deformation and assess any possible correlation with fault orientation along segments of different degrees of geologic inheritance. The results allow us to relate the rupture dynamics of the Maduo earthquake with the long-term evolution of the Jiangcuo fault system.

2. Tectonic and Geologic Setting

The Songpan-Garze terrane, situated in the transition from dilation in central Tibet to compression in the northern Tibetan Plateau, has experienced mainly lateral shear and eastward extrusion (Avouac & Tapponnier, 1993; Tapponnier et al., 2001). Both the GPS velocity field and focal mechanisms of sparse background seismicity suggest that the Maduo hypocenter region is currently under a NE-trending compression and NW extension stress regime (Figure 1b; Wang & Shen, 2020; Xie et al., 2007). The focal mechanisms of the Maduo mainshock and aftershock sequence provide more quantitative constraints, with the principal compressive stresses $\sigma 1$ oriented (N057 ± 18)°/(9 ± 13)°, $\sigma 3$ (N330 ± 18)°/(3 ± 13)° and nearly vertical $\sigma 2$ (Table S1 in Supporting Information S1; Zhang et al., 2022). Consistently, the principal horizontal axes of compressive and dilatation strain rates from the GPS velocity field trend N060° and N300°, respectively, in the epicenter region, parallel to the regional principal stress orientations (Figure 1b). Under the contemporary regional stress field, EW-striking vertical left-

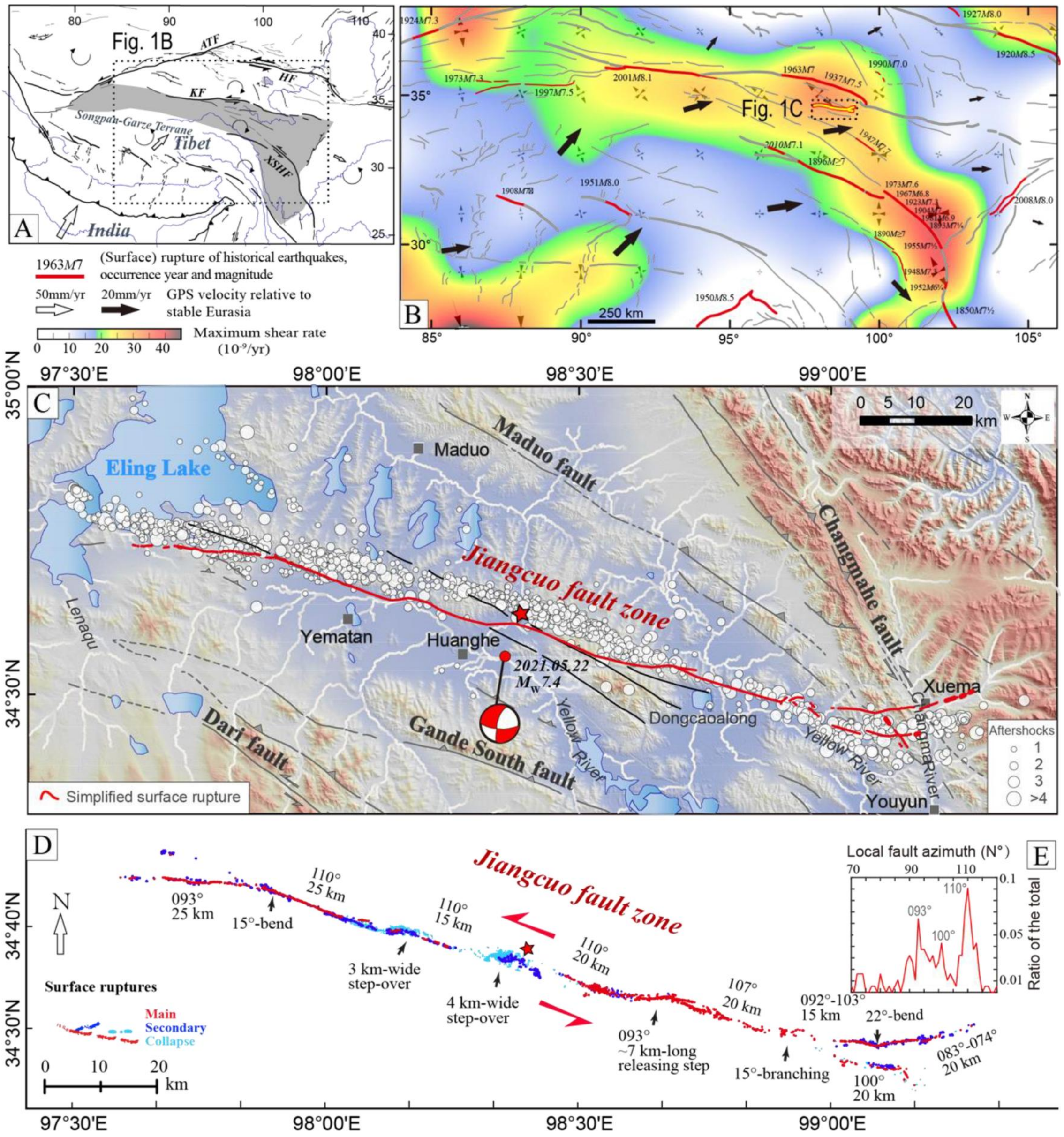

Figure 1. Tectonic and geologic settings of the 2021 M*w* 7.4 Maduo earthquake. (a) Major active faults in the Tibetan Plateau and schematic block rotations. Modified after Tapponnier et al. (2001); Avouac and Tapponnier (1993). ATF: Altyn Tagh fault, HF: Haiyuan fault, KF: Kunlun fault, XSHF: Xianshui He fault. (b) Active faults (gray) and surface-breaking historical earthquakes (ruptures highlighted in red) in the central-eastern plateau. Black arrows denote representative GNSS velocities relative to stable Eurasia. Color contours show the maximum shear strain rate (Wang & Shen, 2020). Principal horizontal axes of compressive and dilatation strain rates, shown in gray, are calculated from the GPS velocity field. (c) Simplified surface rupture map, active faults, and aftershock distribution (Wang et al., 2021). The red dot marks the CENC (https://news.ceic.ac.cn/CC20210522020411.html) epicenter location whereas relocated epicenter (star) and focal mechanism of the main shock are from Zhang et al. (2022). (d) Overall geometry and fractures of the surface rupture zone. Geometrical discontinuities, such as fault bends, step-overs, and branches, are annotated, bounding eight 15–25 km long segments. (e) Histogram of fault local strikes (sampled every kilometer along fault), showing two modal azimuths of N093° and N110°, and a minor one at ∼100°. The histogram also indicates a long-tailed distribution skew toward the more easterly orientation.

lateral faults would be at optimal orientation for reactivation of existing faults if Byerlee-type friction prevails (Byerlee, 1978; Sibson, 1990).

Geologically, the Songpan-Garze terrane comprises strongly folded, often steeply dipping Triassic flysch, with fold axes and bedding parallel to NW- to WNW-striking closely-spaced reverse faults, all inherited from Late-Triassic crustal thickening (Roger et al., 2010; Figure 2). Cenozoic strata are limited, with Quaternary sediments locally around lakes and along tributaries of the Yellow River. The NW-trending structural fabrics exposed

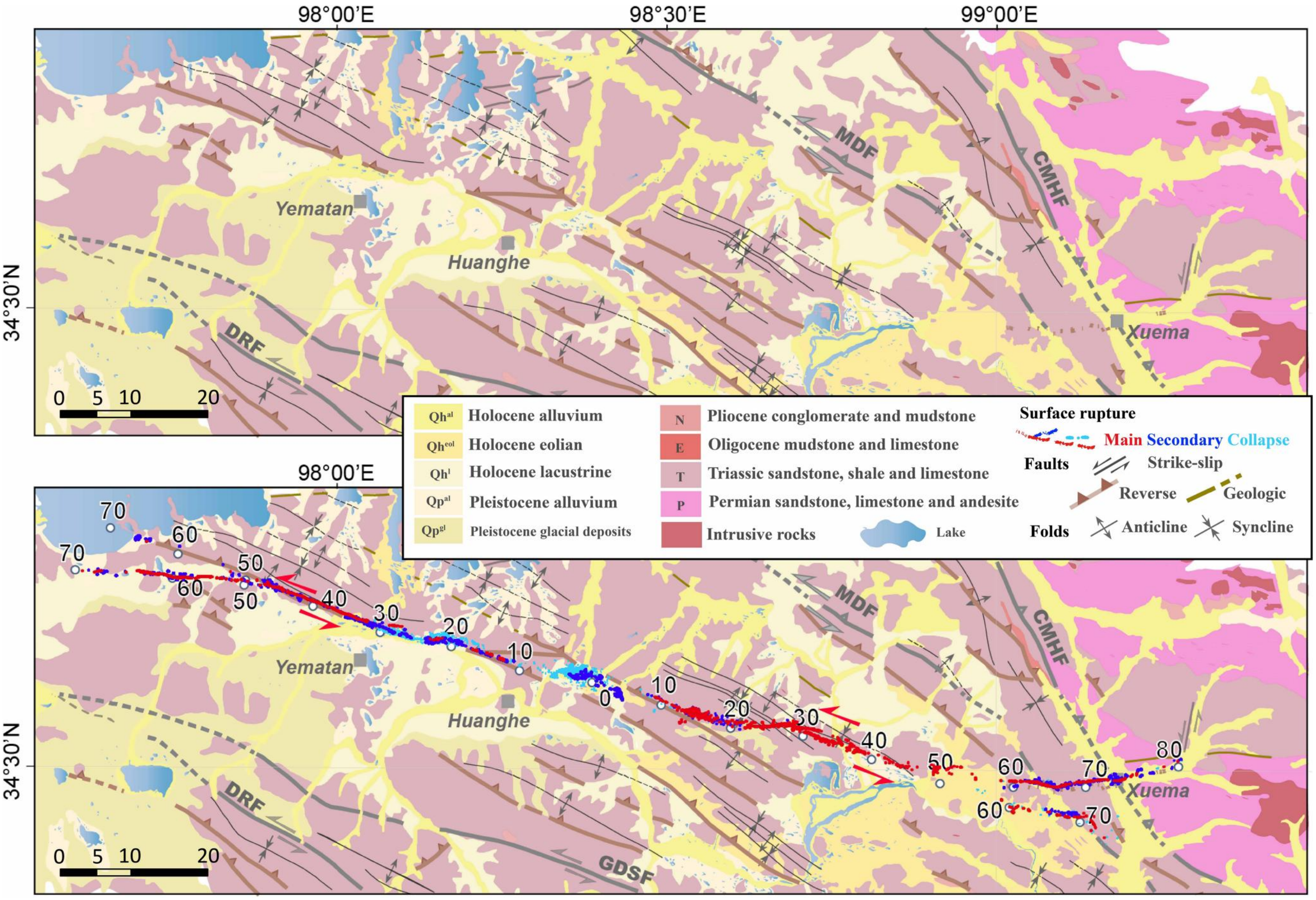

Figure 2. Surface rupture of the 2021 Maduo earthquake superimposed on geological map. For comparison, the upper panel shows only the geological map (Qinghai Institute of Geological Survey, 2010). Numbers along the rupture denote the distance (10 km interval) from the location of the mainshock CENC epicenter projected onto the rupture. GDSF: Gande South fault; DRF: Dari fault; MDF: Maduo fault; CMHF: Changma He fault.

at the surface dominate throughout the upper crust, as indicated by high-resolution seismic wave anisotropy study (Bao et al., 2020) that the fast anisotropy axes in the upper crust are parallel to the thrust-folding structures. The fast anisotropy axis is ~30° clockwise from the EW-trending contemporary maximum shear strain direction at the Maduo epicenter region (Yue et al., 2022). The angle difference indicates the inherited NW-trending reverse faults and folds are not optimally oriented under the contemporary tectonic stress field. The comparison sheds light on the relationship between the evolutionary history of the geological structures and current deformation mode. Block models of plateau deformation predict clockwise rotation of the Songpan-Garze terrane between the E and ESE-striking left-lateral Kunlun and Xianshui He faults (Avouac & Tapponnier, 1993). Thus, the block rotation may set the stage for an evolving fault system, including the Jiangcuo fault, interior of the terrane.

The Jiangcuo fault is considered an immature fault, with its east-growing tip guided by a bend in the Kunlun fault (Pan et al., 2022; Cheng et al., 2023; Li, Li, Hollingsworth, et al., 2023; Figure 1). Campaign-mode GNSS data suggest a slip rate on the Jiangcuo fault of approximately 1.2 ± 0.8 mm/yr (Zhu et al., 2021), an order of magnitude slower than on the >1,000 km-long block-bounding Kunlun and Xianshui He faults, which have been slipping at ~10 mm/yr since 5–10 Ma (Allen et al., 1991; van der Woerd et al., 2000; Wang, 1998). The Jiangcuo fault was unmapped prior to the Maduo earthquake, partly due to a lack of clear tectonic offsets preserved in the geomorphology, suggesting a slow slip rate and long earthquake recurrence time. The total offset on the Jiangcuo fault is ~ 4–5 km in the middle near the epicenter and decreases to ~0.8–1.2 km near the eastern end (Figure 3), consistent with the inference of the eastward growth at the eastern fault end (Li, Li, Hollingsworth, et al., 2023; Pan et al., 2022), a development trying to short-cut the Anyemaqen restraining bend of the Kunlun fault to the east (Pan et al., 2022; Figure 1b). Note that the 3.4 km geomorphic offset of multiple channels are visible on the fault branch, which was not activated during the 2021 Maduo earthquake, south of the epicenter and eastward

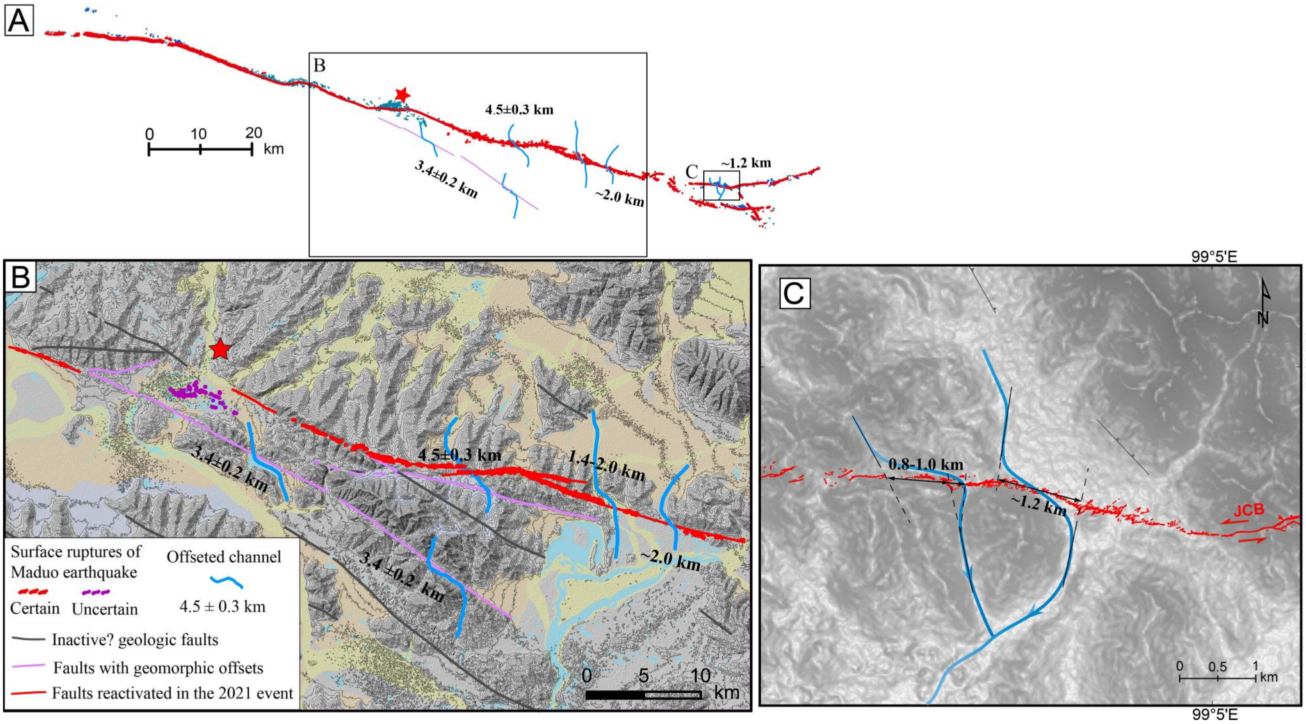

Figure 3. Geomorphic evidence of large left-lateral offsets at different locations along the ruptured fault. Observable cumulative offset decreases eastward from 4 to 5–~1 km. (a) Map view of the surface rupture geometry, showing locations of deflected channels with large cumulative offsets. Star denotes the relocated mainshock epicenter by Cheng et al. (2023). (b) 20 km to the east of the epicenter, a deflected wide valley suggests a cumulative offset of 4–5 km. Also shown are the largest cumulative offsets of ~3.4 km on the branch not activated during the 2021 Maduo earthquake. (c) In the easternmost segment and ~60 km east of the epicenter, deflected river channels recorded a cumulative offset of 0.8–1.2 km.

extension of HHX fault, implying an abandoned fault branch of an evolving fault system. Further to the west, the ruptured faults lie at the bedrock and Quaternary sediments, not showing the cumulative offset. Altogether, the observable largest total slip is about one-tenth of the largest offsets on the Kunlun and Xianshui He faults (Fu & Awata, 2007; Wang, 1998). The Jiangcuo fault is thus presumably much less mature than the Kunlun and Xianshui He faults, by the definition outlined in Manighetti et al. (2007).

The 2021 Maduo earthquake generated a rather simple rupture to the first order. Seismological and remote sensing observations suggest an average of ~2 m left-lateral slip along a relatively simple fault geometry (e.g., Chen et al., 2022; Jin & Fialko, 2021; Wang et al., 2021; Yue et al., 2022). The earthquake initiated near the middle of the rupture, propagated bilaterally at an average velocity of about 2.6–2.8 km/s and possibly reached super-shear velocity in the eastward half (Cheng et al., 2023; Yue et al., 2022). The source time function suggests a relatively simple pulse-like rupture that lasted only about 36 s (Chen et al., 2022). The aftershocks suggest a relatively straight fault geometry for the most part in the middle except for the counter-clockwise bending near both ends, consistent with the remote sensing observations (Figure 1c). The surface rupture length is about twice the expected length of an Mw7.4 strike-slip event on the global average (i.e., Wells & Coppersmith, 1994). The longer rupture length, suggesting a relatively small average slip and thus low stress drop, the relatively straight rupture geometry, and the fast rupture speed, are all surprising characteristics considering that the Maduo earthquake occurred on an immature fault.

3. Materials and Methods

We conducted image acquisition using UAV aerial photogrammetry 3 days after the earthquake, over a 180 km length covering the entire surface rupture zone. We then generated georeferenced orthophoto mosaics, and derived Digital Orthophoto Models (DOMs), Digital Elevation Models (DEMs) based on the Structure from Motions (SfM) algorithm. DOMs with a resolution of 3–6 cm/pixel and high-resolution DEM data with a resolution of 7–15 cm/pixel were generated (Liu-Zeng et al., 2022; Appendix A).

We mapped the surface ruptures in detail, with the help of centimeter-scale resolution DOMs and DEMs, complemented by field observations (Appendix B1). Fractures with length >0.5 m could be identified and mapped out. We categorized these surface fractures as primary, secondary, uncertain, and shaking-related cracks. With mapped fractures, we also quantify the decay of fracture density with distance from the primary fault by the method of Rodriguez Padilla et al. (2022) (Appendix B2). We measured lateral offsets in the field and on the UAV images using linear geomorphic or man-made features, such as channels, grass patches/vegetation lineaments, tire tracks, fences, and roads (Appendix B3). We also measured the vertical offsets using profiles from UAV-derived DEMs, which were field-validated at a few locations where road access is convenient.

We used sub-pixel image correlation of optical satellite imagery to measure the 2D surface strain using Sentinel-2 images and the software COSI-Corr (Leprince et al., 2007; Appendix C; Figure S1 in Supporting Information S1). To measure fault-parallel and fault-perpendicular displacements, we first measured the offset across the fault in the north-south and east-west components. Horizontal slip vectors were then calculated by adding the north-south and east-west components of cross-fault displacements. We then projected the composite horizontal slip vectors into fault-parallel and fault-perpendicular, using the strike of faults segment-wise. We also measured the width of the deformation zone while measuring the east-west component in each swath profile (Figure S1c in Supporting Information S1). The fault-perpendicular width of offsets is a proxy for the extent of inelastic shear strain on either side of the primary, localized fault trace.

4. Results

4.1. Geometry of the Surface Ruptures

We used UAV-based centimeter-resolution orthophotos and Digital Elevation Models (DEMs), complemented by field observations, to map the surface rupture zone in detail. These investigations reveal a 158 km-long surface rupture trending 106° in the middle and EW-striking branches at both the eastern and western ends (Figure 1c). The cm-resolution images allow us to recognize and map exhaustively surface fractures (length >0.5 m). The surface rupture zone consists of one or multiple zones of distributed fractures, tension gashes, small grabens, push-ups, and mole-tracks (Pan et al., 2022; Ren et al., 2022; Yuan et al., 2022; Figure 1d and Figure S2 in Supporting Information S1). Despite the simple first-order geometry, our detailed observations show a segmented surface rupture trace, separated by km-scale fault bends, step-overs, and branches. These geometrical complexities lead us to distinguish eight 10–25 km long segments. A similar segmentation length scale has been observed along other recent ruptures in Tibet and interpreted to reflect control by the thickness of the seismogenic crust (Klinger, 2010). Near the epicenter and to the west, three ∼N110°-striking segments are separated by 3- to 4 km-wide trans-tensional step-overs, while the westernmost segment strikes N093°. East of the epicenter, the strike of the surface rupture changes gradually toward a more easterly orientation, from ∼N110° to N107° and then to ∼N100°. A northern branch splays off anti-clockwise, rotating to ∼N092° and further to N074° at its eastern tip. The histogram of local fault orientation averaged over 1 km-interval peaks at N110° and N093° and is skewed toward a more easterly orientation (Figure 1e).

The segments sorted according to the two main orientations differ in geologic inheritance. Structurally, the N110°-striking segments coincide with WNW-striking and north-dipping reverse faults, inherited from Late-Triassic crustal thickening of the Songpan-Garze terrane (Qinghai Institute of Geological Survey, 2010; Roger et al., 2010; Tapponnier et al., 2001). In contrast, the more easterly-oriented segments cut through the NW- to WNW-trending rock units and structural fabrics (Figures 1c and 2). At the very eastern end, the branched rupture cut across pre-existing terrane-defining thrust faults at a high angle, 40–60° (Figure 2). The 093°-trending tip splays at both rupture terminations branch toward the extensional quadrants of the left-lateral strike-slip Jiangcuo fault.

Three types of measurements show consistently that the deformation zone is narrower across the ∼N093°-striking fault segments (light blue shading in Figure 4) and widens along the ∼N110°-trending ones. The surface rupture width, defined as the width of the envelope of all mapped fractures on UAV orthophotos, is the widest in the middle and narrows toward the two rupture ends (Figure 4c). It averages 73 m on the N093°-striking splay faults at two rupture ends and 314 m on the N110°-striking sections. Another metric of how diffused deformation is the width of the surface deformation zone captured from the COSI-Corr correlation of Sentinel 2 optical satellite images (Antoine et al., 2021; Michel & Avouac, 2006; Milliner et al., 2015, 2021). Similarly, the width of the relative surface displacement zone is narrower on the ∼EW-striking segments as well (Figure 4d). At the rupture termini of

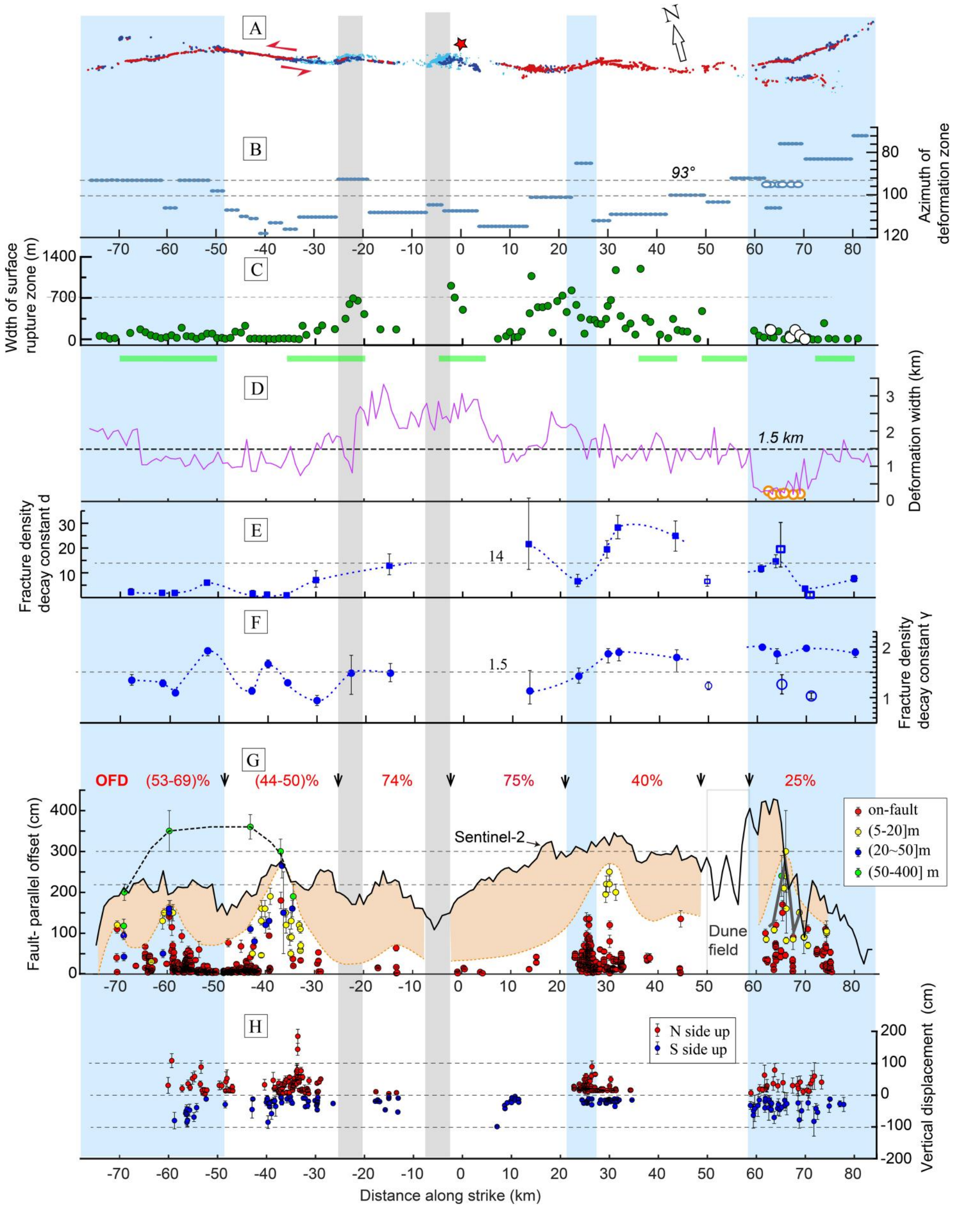

Figure 4. Along-strike variation of surface rupture characteristics. Along-strike distance is measured relative to the epicenter. Light blue shading denotes the EW-striking and optimally oriented fault splays and bends, whereas trans-tensional step-overs without through-going surface rupture in gray. (a) Map-view of the surface rupture is rotated ∼20° counter-clockwise such that N110° is parallel to the horizontal axis of panels (b) through (h). (b) Orientation of surface displacement zone indicated by the EW-component of optical image correlation, measured every 2–3 km along the fault. Open symbols for the southern branch. The width of (c) surface rupture zone and (d) deformation zone is relatively small along EW-striking segments. Green bars denote the sections, where the rupture occurred in alluvium. (e) and (f) Variation in power law inner corner *d* and decay constant γ of coseismic fracture density, which were defined in Rodriguez Padilla et al. (2022). (g) Comparison of coseismic left-lateral surface displacements measured with different methods. Filled circles denote offsets on discrete faults measured in the field or on UAV images. The orange dashed lines denote the envelope of surface offsets measured over <50 m-wide apertures. The black line denotes the displacement curve from the sub-pixel image correlation of pre- and post-earthquake Sentinel-2 optical satellite images. The orange shading denotes the difference in displacements by the two methods, indicating the degree of off-fault deformation with the ratios shown for major segments. Error bar omitted for the sake of clarity. Within 60E−70E km, open symbols in panels A through F and the black dashed curve in panel G represent data on the southern branch. Off-fault deformation (OFD) ratios are calculated in sections separated by geometric discontinuities. The ratio for the westernmost two sections could be higher. (h) Vertical displacements along the fault, measured from UAV orthophoto-derived DEMs. Alternation of north-side-up and south-side-up suggests a nearly pure strike-slip style.

the two long EW-striking segments (67–76W and 73–83E km), the deformation width increases, instead of narrowing as the surface rupture and coseismic slip die out. Note, however, for a 10 km-long section in the middle of the N110°-striking segment (32–42W km), the surface rupture is as narrow as on the ~EW-striking segments.

A third indicator of the extent of diffuse deformation is the power-law decay of fracture density with distance from the fault. The inner corner of the power-law *d* is smaller on the EW-trending than WNW-trending segments (indicating a narrower mapped fracture zone, see Figure 4e), consistent with the relationship between rupture zone width and fault orientation. The decay exponent γ fluctuates around ∼1.5 on average and is generally larger in the sections east of the epicenter than to the west (Figure 4f), indicating a narrower zone of distributed fracturing to the east. All three indicators are consistent with one another and may be used as proxies for quantifying the long-strike variation in the coseismic deformation zone. The narrow EW-striking segments include two splay faults at rupture ends (50–70W km and 60–80E km) and one releasing bend (21–28E km), contrary to anticipated distributed deformation at such structural complexities along strike (Mitchell & Faulkner, 2009; Sieh et al., 1993). The ∼EW strike, optimal for the Mohr-Coulomb failure criterion under a regional N057° horizontal σ1 background stress (Sibson, 1990) appears to play a more important role in controlling the width of coseismic deformation than structural complexity.

4.2. Coseismic Surface Slip and Off-Fault Deformation

We compiled 833 measurements of left-lateral slip along the ruptured fault, including both field (311), and UAV-derived (522) measurements (Figure 4g and Table S2). The offset is generally smaller than 1.5 m, and peaks at 2.5–3 m east of the epicenter (∼30E and ∼65E km) on EW-trending segments. Surface slip tapers locally at geometric discontinuities, such as the extensional step-overs (2–7W and 20–25W km) and fault junctions (45–52W and 50–55E km). Field-measured surface slip is the smallest within 20 km of the epicenter, where surface rupture is minor and discontinuous cracks are sometimes not easily distinguishable from shaking-related fissures, indicating incomplete rupture to the surface at this location (Figure 4a). Interestingly in this section, the rupture velocity is the slowest, and the shallow slip deficit is the largest (Cheng et al., 2023; Wei et al., 2022; Yue et al., 2022).

Our measurements of horizontal surface slip, which include 6–8 times more observations than previous studies (Pan et al., 2022; Yuan et al., 2022), include a range of apertures, from those on-fault or within the fracture zone (0–20 m in width), across the visible fracture zone (20–50 m), to the long-range (>50 m), up to 400 m across the fault (Figures 4g and 5a). The location of left-lateral offsets that we measured is unevenly distributed along the fault, depending on the availability of offset piercing lines, which include geomorphic markers, vegetation lineaments, and man-made features, such as vehicle tire tracks and fences (Figures S3 and S4 in Supporting Information S1). It is essential to attribute an aperture to each measurement, as measurements made on discrete fractures easily underestimate the total surface slip (Figure 5a). This occurs because the left-lateral offset is accommodated by distributed shear across the zone of trans-tensional cracks (mostly >20 m wide) that are at a relatively high angle (∼40°) to the general fault strike (Figure S2 in Supporting Information S1).

We used sub-pixel correlation of Sentinel 2 optical satellite images to estimate the horizontal displacement near the fault, decomposed into fault-parallel and fault-normal directions. The left-lateral offsets provided by image correlation display along-strike variation correlative with geometric discontinuities, a similar pattern as field- and UAV-based on-fault measurements (Figure 4g). The left-lateral slip is ∼2.3 m on average and ∼4.2 m maximum, respectively. Local slip minima occur at segment boundaries, such as step-overs and fault bifurcation points, in agreement with the pattern shown by our UAV and field-based measurements. The slip is in general larger east of the epicenter (∼3 m) than to the west (2.2 m). The maximum slip occurred east of the bifurcation (50E km) on the generally EW-striking curved eastern terminal splay fault, instead of on the simple and straight 110o-striking mid-western sections, indicating that fault orientation plays a role. The general pattern of pixel-correlation coseismic slip is broadly comparable with the geophysical finite fault solutions of Yue et al. (2022); Chen et al. (2022) at the shallowest depth, with some differences locally (Figure 5b).

Measurements by sub-pixel image correlation are associated with a wider aperture (100–1,000 m) than field- and UAV-based measurements, over the visible fracture zone (mostly >20 m wide). A comparison of offsets from two approaches quantifies the off-fault deformation or the percent of the total displacement not accommodated by the primary fault strands (Antoine et al., 2021; Michel & Avouac, 2006; Milliner et al., 2015; Vallage et al., 2015). The off-fault deformation (OFD) ratio is in general smaller east of the epicenter (25%–42%) than west of it

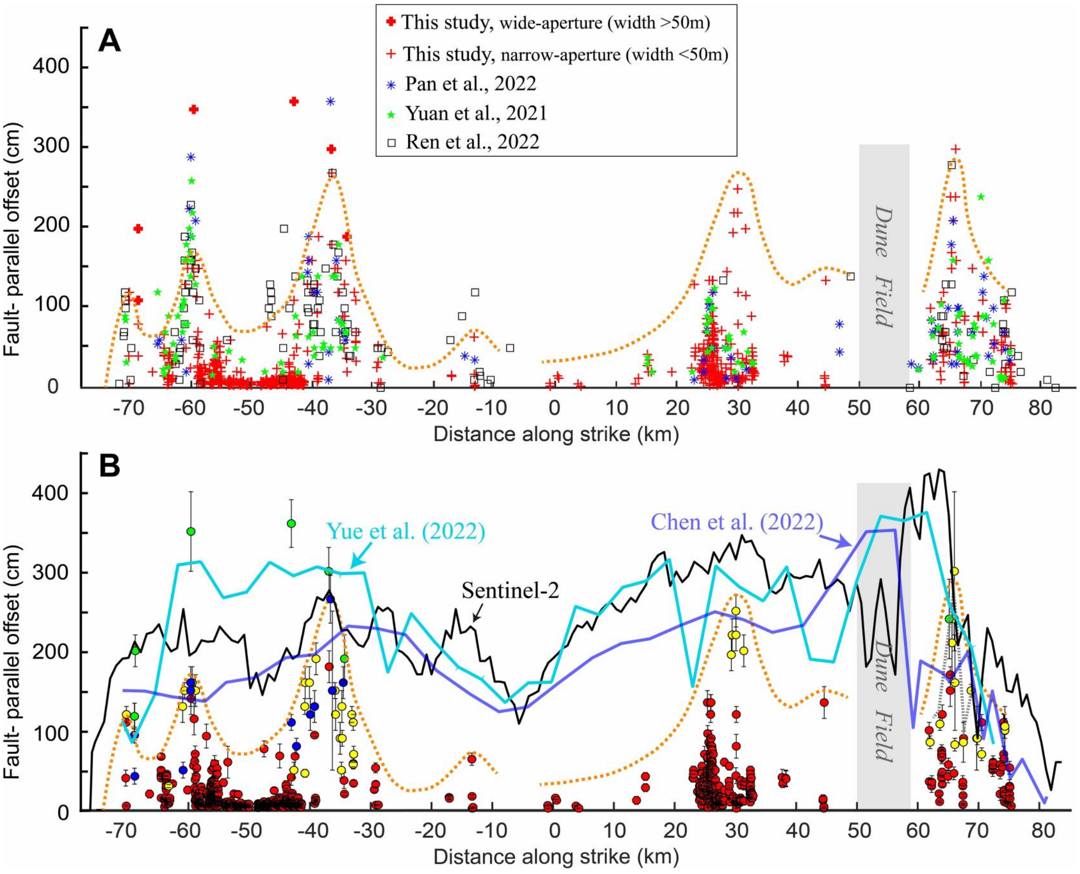

Figure 5. Comparison of our field/UAV image-based measurements with published geologic (a) and geophysical (b) results. Geophysical results of Chen et al. (2022); Yue et al. (2022), of which the shallowest 1–3 km depth pixels of finite-fault inversion are shown in color curves. For geologic field measurements, it is essential to attribute an aperture to each measurement. Our measurements include a range of apertures, from those on-fault or within the fracture zone (0–20 m in width), across the visible fracture zone (20–50 m), to the long-range (≥50 m), up to 400 m across the fault. Note that the large coseismic slip (∼3.6 m) at ∼30W km by Pan et al. (2022) was measured with powerline poles projected over ∼100 m width across the fault, which includes off-fault deformation. At the same site, we measured 2.7 ± 0.3 m (on-fault) and 3.0 ± 0.3 m (off-fault included).

(∼50%), indicating more localized deformation in the east (Figure 4g). The ratio is the smallest at the eastern branching end. The average OFD ratio is 46%, reaching up to 75% near the epicenter, where the rupture is largely blind. In addition, other long-range piercing lines (∼100 m apertures) such as ranch fences or powerline poles, also record distributed off-fault deformation going beyond the fracture zone (Figure S4 in Supporting Information S1). At six locations in the western end, the OFD ratio indicated by these man-made features is 25%–62% over a 60–400 m wide zone, among which four are consistent with that captured by sub-pixel image correlation whereas two are larger (Figure 5b). The ranch fence-derived offsets can be over-estimated if the assumption of a straight-line geometry prior to the earthquake is not met. Alternatively, the sub-pixel correlation results of Sentinel 2 optical satellite images under-estimated the total surface slip due to a large smoothing window (80 m-resolution) and larger noise in the western end, where rupture runs through the swampy alluvium near the Eling Lake.

Rupture through alluvium of the Yellow River meanders, may partially explain the relatively high OFD ratios in the westernmost section. Besides that portion of the rupture, we find no strong correlation between near-surface lithology and OFD ratios, surface rupture width, or fracture density decay (Figure 4), consistent with findings from the 2019 Ridgecrest earthquake (Rodriguez Padilla et al., 2022). Our study suggests that differences between geologic and sub-pixel correlation methods may not directly amount to the magnitude of off-fault strain because there is missing slip measured in the narrow, on-fault rupture zone. The comparison of geologically measured surface slips of different apertures shows that surface slip across discrete fractures normally underestimates the

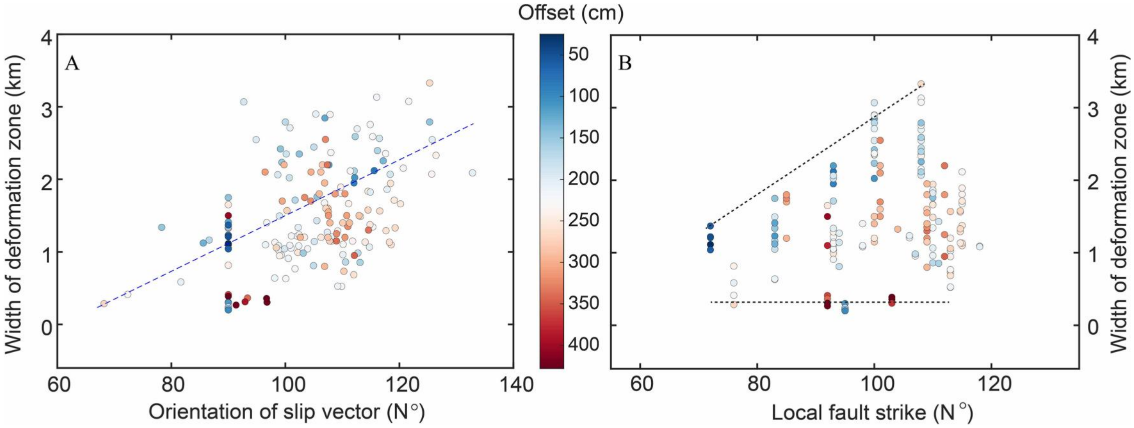

Figure 6. Width of the surface deformation zone is plotted against the orientation of (a) slip vector and (b) local fault strike. Both the width and slip vector are based on the results of pre- and after-earthquake image correlation. The data points are color-coded by the COSI-Corr derived coseismic slip. The positive correlation in panel A suggests that the deformation zone is narrower when the slip vector orients more easterly. The correlation of width with local fault strike is less prominent, yet the maximum width of deformation is smaller on the N080-090° than on the N110°-striking faults.

total surface slip (Figures 4g and 5a). Thus, the abnormally high OFD ratio of 80%–90% in Li, Li, Shan, and Zhang (2023) is likely an overestimation, which used the underestimated field measurements of slip in Yuan et al. (2022) for the comparison.

5. Discussion

5.1. Eastward Fault Growth With Stress-Optimally Oriented Segments

Surface rupture geometry and coseismic slip distribution show consistently that deformation on the ~N093°-striking segments is more localized, with narrower rupture and deformation zones, and less off-fault deformation than on the N110°-striking segments. At the eastern end with branched faults striking N083-100°, summed deformation width of both branches suggests narrower and more localized deformation than on N110°-striking segments, despite being horsetail rupture termini. In addition, the magnitude of the coseismic slip does not play a role in the relationship between the deformation zone width and orientation of the horizontal slip vector or the local fault strike (Figure 6).

Our observations suggest that the orientation of the fault segment relative to the regional tectonic stress is a primary factor controlling strain localization. Under the current stress regime (horizontal σ1 and σ3, oriented N057° and N330°, respectively), the ~N093°-striking segments are more favorably oriented than the N110°-striking ones, as Mohr-Coulomb failure theory predicts that faults form at 30° from the direction of maximum compression, assuming a standard coefficient of friction of 0.6 (Sibson, 1990; Zhang et al., 2022). The most favorable inclination angle to σ1 (~30°) explains the narrower deformation zone on the ~N093°-striking segments for a dominantly strike-slip fault, that is, alternating equally north side up and south side up in the vertical component (Figure 4h). Most of the anticipated inelastic strain would collapse onto the fault in the form of localized slip, leaving a minimum amount available for the generation of off-fault deformation during the dynamic rupture process (Templeton & Rice, 2008).

Consistently, faults with an optimal dip angle relative to regional stress were found to correlate with a narrower surface rupture zone than misoriented ones in the 2010 Mw 7.2 El Mayor-Cucapah earthquake (Teran et al., 2015; Fletcher et al., 2020). Teran et al. (2015) reported positive correlations between rupture zone width, fault zone width/architecture, and fault misorientation. Among various factors affecting the rupture width, Fletcher et al. (2020) showed that fault misorientation and protolith are the main factors that control both rupture zone width and overall fault zone architecture, whereas the cumulative slip or fault maturity was the least important factor in their analysis.

A systematic change in the strike of the ruptured segments suggests that the eastward propagation of the Jiangcuo fault system evolves progressively toward a more stress optimal orientation (Figure 7c). In the mid-to-western sections (45W–15E km), the rupture cascaded through a series of N110°-striking inherited and less favorably

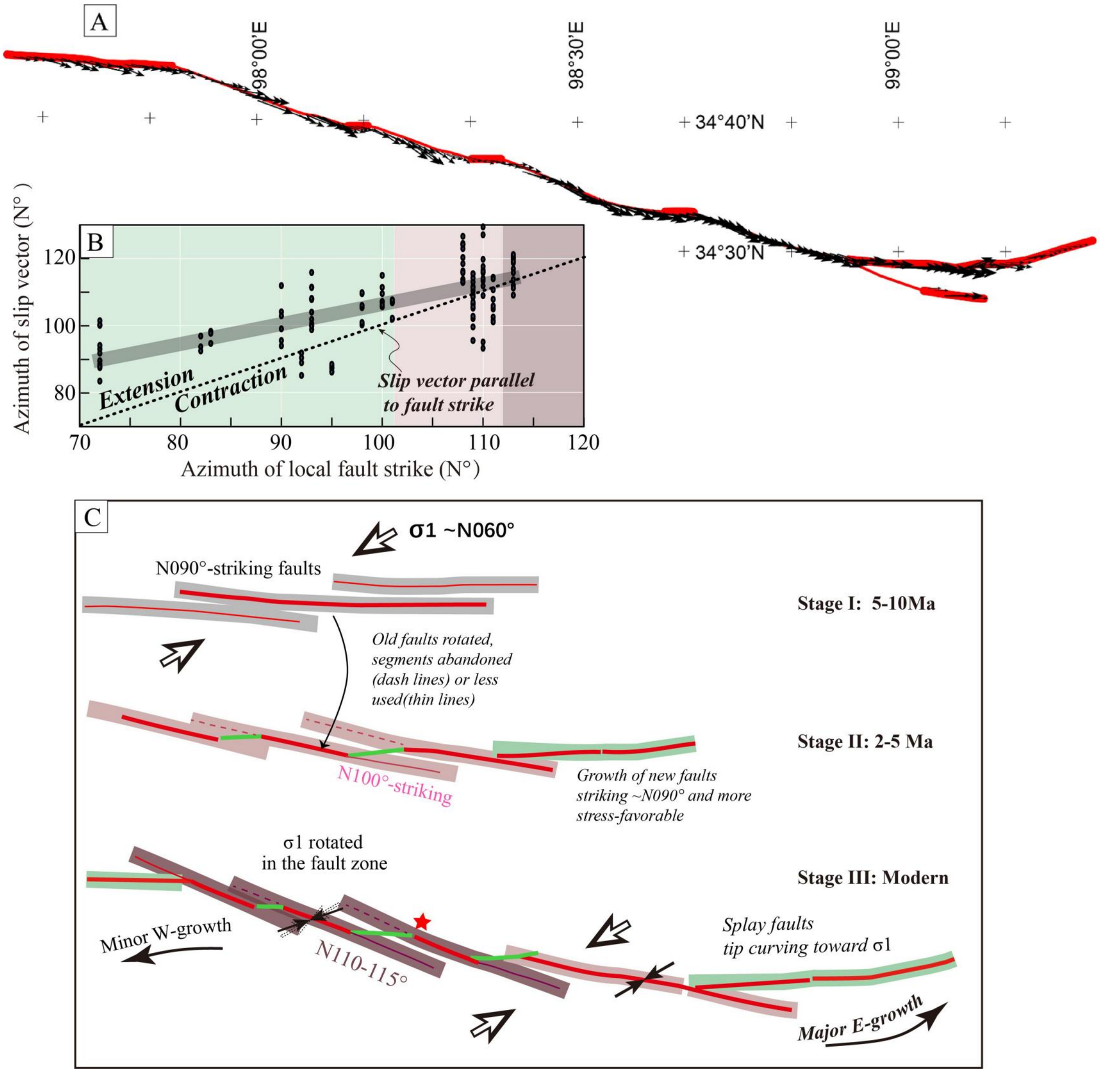

Figure 7. Model of fault growth toward stress-favored orientation. (a) Horizontal slip vectors, composed of EW and NS components from image correlation, are shown in the map view, representing the motion of the southern side of the fault relative to the northern side. EW-striking fault segments are highlighted in bold red lines. (b) Relationship between azimuth of horizontal slip vector and local fault strike indicates more extensional components on more easterly-trending segments, which are more favorably oriented with the regional principal stress direction (~N057°). Background shading in green, pale brown, and brown denotes the stress-favorable, unfavorable, and severely misoriented fault local strike, respectively, by the definition in Sibson (1990). (c) Earthquake rupture scenarios on an eastward-growing fault system with older faults being rotated clockwise to progressively unfavorable orientation and new faults being formed on planes favored by stress orientation.

oriented faults, linked by more favorably oriented segments (Figure 4b). East of the epicenter, the ruptured segments dissect the NW-trending Triassic rock units and subparallel faults and folds. Fault segments strike more easterly stepwise from N110° to N107°, then at the eastern end to N100° on the southern branch and N083-092°on the northern branch (Figure 1d). The northern strand, longer than the southern one, branches off at an angle of 10–20° and then curves further toward σ1, a characteristic orientation of a newly formed shear fracture or tip splay fault (Scholz et al., 2010; Sibson et al., 2011). This is consistent with the eastward expansion of the Jiangcuo fault (Pan et al., 2022) (Figure 7c). Thus, the Maduo earthquake ruptured fault segments with different levels of structural maturity, where the fault is the least mature at the easternmost end. This is a rare opportunity to observe rupture spanning fault segments in a range of structural development phases in a single earthquake, partly due to a combined effect of a long rupture in the growing fault tip zone on a slow-moving, low-total slip fault.

Clockwise block rotation of the Songpan-Garze terrane between the left-lateral fast-slipping Kunlun and Xianshui He faults (Avouac & Tapponnier, 1993) provides a viable mechanism can explain the progressive misorientation of older N110°-striking geologic faults to nearly the lock-up angle 50–60° from the σ1 trend of ~N057° for a friction coefficient range of 0.6–0.85 (Byerlee, 1978; Sibson, 1990). Paleomagnetic study in the Songpan-Garze terrane is lacking due to a scarcity of Cenozoic sedimentary basins and volcanics. However, given ∼10 mm/yr slip rates of two bounding faults and ∼300 km width of the block, the rotation rate could be ∼2°/Myr (Appendix D). With this rate, it would take ∼10 Myrs to accumulate 20° total rotation on the 110°-striking segments, consistent with the initiation time of the Kunlun and Xianshuihe faults (Fu & Awata, 2007; van der Woerd et al., 2000; Wang, 1998). The Jiangcuo fault was hypothesized to be a recently formed (2–3 Ma?) branch of the Kunlun fault system to shortcut the Anyemaqen restraining bend and a kink in geometry on the main strand (i.e., Pan et al., 2022). While the eastward growth of the Jiangcuo fault system may be guided by the Anyemaqen bend, the initiation of the Jiangcuo fault does not have to be young. At a regional scale, the Jiangcuo fault is one of the series of the secondary faults cutting diagonally across the Songpan terrane, bridging the Kunlun and Xianshuihe faults (Figure 1). It is reasonable to infer that the initiation of the Jiangcuo fault is coeval to the Kunlun and Xianshuihe faults if they belong to the same large-scale fault system. The initiation of the Jiangcuo fault and the associated controversy are yet to be further explored.

Tectonic rotation suggests a non-stationary fault configuration, setting the stage for the seismogenic Jiangcuo fault zone to evolve in geometry. During the process, new splay faults formed on the optimal plane for faulting that is, striking ∼N093° (Figure 7c). Consistently, the Maduo aftershocks form a more easterly-trending fabric, more continuous than the segmented surface rupture, suggesting new development of the fault system at depth shortcutting the geometric irregularities (Figure 1c). Tectonic rotation from an initially optimal orientation was considered as a compelling mechanism to explain the high-angle conjugate faults failed in the Landers, Hector Mine, and Ridgecrest earthquake ruptures (Fialko & Jin, 2021; Milliner et al., 2021; Ron et al., 2001) or the long-term fault kinematics in California (Thatcher & Hill, 1991).

5.2. Effect of Stress-Favorable Orientation on Rupture Characteristics

Eastward fault rotation toward a stress-favorable orientation correlates with along-strike difference in rupture speed, coseismic slip, and off-fault deformation in a unified framework. The eastern half of the bilateral rupture, while on less mature but more stress favorably-oriented faults, appeared to be more energetic. The rupture may have reached super-shear velocities locally 30–50 km east of the epicenter, coinciding with a gap in aftershocks (Cheng et al., 2023; Yue et al., 2022). The east-propagating rupture bifurcated at the fault junction 50 km east of the epicenter and resulted in simultaneous rupturing on two small-angle forked faults and radiating more high-frequency waves than elsewhere (Wei et al., 2022). In contrast, the west-propagating rupture, which mainly followed the N110°-striking, stress-unfavorable and older inherited faults, was overall slower, with an average speed of only ∼60% of the eastward rupture (Cheng et al., 2023; Yue et al., 2022). The coseismic slip on the surface and at depth is smaller on less favorably oriented faults, with a higher percentage of off-fault deformation. Geophysical inversions of coseismic slip at depth show similar asperities of large slip patch occurring on the ∼EW-striking segments (e.g., Jin et al., 2023; Yue et al., 2022). One interesting exception is for a 10 km section (32–42W km) on the N110°-striking segment, where the surface deform zone and rupture zone are similarly narrow to the EW-striking segments and the coseismic surface slip reaches a local maxima. The dynamic effect was proposed to explain this abnormal phenomenon (Antoine et al., 2023).

Coseismic failure on a suite of faults from favorable to unfavorable orientations can be used to infer the frictional stress state on the fault plane (Fletcher et al., 2016, 2020; Rodriguez Padilla et al., 2022). The misaligned N110°-striking fault segments ruptured concurrently with the favorably oriented faults, but with a smaller slip and slower rupture velocity (Jin et al., 2023; Wei et al., 2022; Yue et al., 2022). This indicates that the less favorably oriented fault segments, though more mature, fail under a low level of shear-to-normal stress ratio (Thomas & Bhat, 2018; Xu et al., 2015). Conversely, a higher shear-to-normal stress ratio on structurally less mature, but more favorably oriented (N093°-striking) faults resulted in more localized deformation (Duan & Day, 2008; Thomas & Bhat, 2018). In addition, the transition from an N110°-striking segment to an N093°-striking segment represents a releasing bend under left-lateral slip. Along the EW-oriented fault segments, the horizontal coseismic slip vectors indeed indicate a larger component of extension (Figures 7a and 7b). Surface rupture of the Maduo earthquake is dominantly expressed as “tension gashes,” transtensional and *en echelon* T fractures, making ∼40° angle with the local fault strike (Figure S2 in Supporting Information S1), different from the typical Riedel R-shears observed in clay-box experiments and often reported during field surveys of coseismic ruptures during strike-slip events (Tchalenko, 1970).

The extensional component could dynamically reduce normal stress (unclamping) and hence fault strength for the following N093°-striking segment, with the potential to promote rupture acceleration associated with an off-fault damage gap (Duan & Day, 2008; Dunham et al., 2011). Quasi-static models (with Mohr-Coulomb-type yield criterion) along a rough or wavy fault, on the contrary, predict more extensive off-fault damage around an extensional step, because of the slip-induced tensile normal stress change around that location (Chester & Chester, 2000; Lindsey et al., 2014). However, in such models, simultaneous, quasi-static, slip is prescribed along the entire fault under a constant friction, such that any dynamic effects (rupture propagation, frictional weakening) would be ignored. The combined effect of static tectonic stress and dynamic unclamping during earthquake rupture would explain the faster rupture speed, the largest coseismic slip, and the least percentage of off-fault deformation on the EW-striking segments (Figure 4g).

Previous studies have argued that faster rupture speeds, to even super-shear speeds, should occur along smoother and structurally more mature faults rather than geometrically rough and immature faults (Bruhat et al., 2016; Guo et al., 2023; Perrin, Manighetti, Ampuero, et al., 2016). By contrast, our observations from the Maduo earthquake suggest that the structurally less mature fault, if more stress-optimally oriented, promoted a faster and more energetic rupture, more localized deformation, and larger coseismic slip. We attribute this to its more favorable orientation relative to the regional tectonic stress and its reduced fault strength promoted by dynamic unclamping. Thus, the Maduo earthquake suggests that the structural simplicity of a fault is not the only factor that contributes to faster rupture speed and more localized deformation.

The degree of fault alignment to the stress field can play a more important role on rupture dynamics than fault maturity when both factors are at play. This may be a general mechanism underlying how rupture chose its optimal path through a complex network of faults with different orientations or dips (Fletcher et al., 2016; Hubbard et al., 2015; Ron et al., 2001; Sibson et al., 2011). For instance, it can explain why sub-horizontal décollements coexist with steeply oriented splay faults in subduction zones and continental fold and thrust belts (Hubbard et al., 2015): ruptures choose to curve upward from the more mature, less optimally oriented décollement to less mature, but more optimally oriented, splay faults. Our results have important implications for better quantifying fault displacement hazard and lifeline design, for which the critical parameter of rupture and deformation width (Petersen et al., 2011; Sarmiento et al., 2021) would be better informed when geologic inputs of fault azimuth and its degree of optimality within contemporary stress field are considered.

6. Conclusion

The 22 May 2021 Maduo earthquake occurred in the east-growing tip zone of the slow-moving, low-total slip Jiangcuo fault, providing a rare opportunity to observe rupture spanning fault segments in a range of structural development phases in a single earthquake. We combine field and multiple remote sensing techniques to map the surface rupture of the Maduo earthquake at cm-resolution and to document comprehensively on-fault offsets and off-fault deformation. The 158 km-long surface rupture consists of misoriented structurally inherited N110°-striking segments and younger optimally oriented N093°-striking segments, relative to the regional stress field. Surface rupture geometry and coseismic slip distribution show consistently that deformation on the ~N093°-striking segments is more localized, with narrower rupture and deformation zones, less off-fault deformation, and possibly faster rupture speed than on the N110°-striking segments. A systematic change in the strike of the ruptured segments suggests that the eastward propagation of the Jiangcuo fault system evolves progressively toward a more stress optimal orientation. These results are in contrast with previous findings showing more localized strain and faster rupture speed on more mature fault segments; instead, our observations suggest that fault orientation with respect to the regional stress can exert a more important control than fault maturity on coseismic rupture behaviors when both factors are at play.

Appendix A: UAV Image Acquisition and Building 3D Topography

We began our data acquisition using aerial photogrammetry by UAV 3 days after the earthquake. Between 24 May and 15 June 2021, more than 34,302 low-altitude aerial photos were acquired over a 180 km length, covering the entire surface rupture zone. We combined two types of UAVs with different flight speeds and corresponding flight altitudes to maximize survey efficiency and resolution. We used the CW-15 VTOL fixed-wing UAV, with speeds up to 90 km/hr, for covering larger zones efficiently and with parameters set for target image resolutions of ~3–6 cm/pixel. For georeferencing, we used the Chinese Continuously Operating GNSS Reference Stations

(CORS) within the flight zone and the adjacent region as the ground reference frame. The real-time kinematics (RTK) base station provided the link between the drone and CORS and used GPS PPK (post-processed kinematic) algorithm to get the positioning, achieving an accuracy of cm in kinematic and mm in static. More details about data acquisition and processing are described in Liu-Zeng et al. (2022).

We used Agisoft software (PhotoScan) to generate georeferenced orthophoto mosaics, and then derived Digital Orthophoto Models (DOMs), Digital Elevation Models (DEMs) based on the Structure from Motions (SfM) algorithm. DOMs with a resolution of 3–6 cm/pixel and high-resolution DEM data with a resolution of 7–15 cm/pixel were generated from the hybrid fix-wing UAV data acquisition. Using the ArcGIS platform, we built derivative products, such as hillslope maps, aspect maps, shaded relief maps, and topographic contour lines.

Appendix B: Surface Rupture Mapping and Deformation Metrics Measurement

B1. Mapping of Surface Ruptures

We used centimeter-scale resolution DOMs and DEMs, complemented by field observations, to map the surface ruptures in detail. Computer-based mapping is facilitated by helpful information such as contour maps, slope, and slope aspects, and surface roughness, which can be obtained by processing high-precision DEMs. We adjusted the image contrast and color rendering to increase the visibility of surface rupture features and traced the geometry of fractures.

Using ArcMap software and the maps mentioned above, 10 mappers spent more than a half month working full-time to develop the detailed maps of the Maduo surface rupture. To avoid possible omission or duplication, we divided the mapped area into kilometer-size grids for mapping jobs, which is also convenient for double-checking the results. For each grid, we searched for mappable cracks under a pre-set scale, for example, 1:1000 scale, and then searched for smaller features with increasingly enlarged scales of 1:500 and 1:300.

With these strategies and data sets, fractures with length >0.5 m could be identified and mapped out. We categorized these surface fractures as primary, secondary, uncertain, and liquefaction fractures (to distinguish tectonic-induced fractures from those due liquefaction or gravitational sliding). Ambiguous categories of fractures were further field validated during the subsequent field trip in September 2021.

B2. Fracture Density Decay Constants

We quantify the decay of fracture density with distance from the primary fault by the method of Rodriguez Padilla et al. (2022). We measured the nearest distance between each fracture in the fracture maps and the primary fault. Fractures were discretized into evenly spaced points at 1 m increments so that fracture length does not bias the fracture counts. Once the minimum distance for each fracture was computed, we binned them into 100 bins per data set that are log-spaced from the origin to the furthermost point in the data set. We then normalized each of the bins by the bin size and by the rupture length of the primary fault for each section. We then fit the data with an inverse power-law using the expression in Powers and Jordan (2010), using an implementation of the affine-invariant ensemble sampler for Markov Chain Monte Carlo and assuming that $\nu(x)$ within each bin samples a Poisson distribution. We applied a uniform distribution to ν_o(100 to 10-5 fractures per square meter), d (0–3,000 m), and γ(0.5–2) as our priors. We run the fits for 10,000 iterations, preceded by a burn-in phase of the same length. We used an ensemble of 200 walkers.

B3. Measurements of Lateral and Vertical Offsets on Discrete Fault

We measured lateral offsets in the field and on the UAV images using linear geomorphic or man-made features, such as channels, grass patches/vegetation lineaments, tire tracks, fences and roads. Our measurements, a total of 833, include those made over narrow apertures (i.e., across the en-echelon cracks), and wide apertures, that is, long piercing lines, such as roads, fences and electric lines, projected meters on either side of the fault (Table S2). Offsets measured directly on fracture or fracture zones are often centimeters to decimeters and smaller than the 5–50 m wide-aperture measurements, suggesting coseismic deformation is not fully captured by discrete fractures. Reconstruction of pre-earthquake geometry of long (>50 m) man-made features allows detection of distributed yielding and off-fault deformation.

We also measured the vertical offsets using profiles from UAV-derived DEMs, which were field validated at a few locations where road access is convenient. We used ArcGIS 10.3 to extract topographic profiles that are perpendicular to the local surface rupture zone along fault and to measure the hanging wall to foot wall separation directly. We focused on simple sites where the displaced geomorphic surfaces on both sides of the faut are of the same age so that the measured throw values are reliable. We have a total of 301 measurements of vertical displacements (Table S3).

Appendix C: Subpixel Image Correlation, 2D Deformation Field and Off-Fault Deformation

To measure the 2D surface strain, we used sub-pixel image correlation of optical satellite imagery to retrieve horizontal displacement maps of the coseismic rupture following the approach of Milliner et al. (2021). We used 22 Sentinel-2 images and the sub-pixel correlation software COSI-Corr (Leprince et al., 2007) to correlate the pre- and post-earthquake images to produce a map of horizontal surface displacement (see Table S5 in Supporting Information S1 for list of image metadata). The images are orthorectified using the satellite ancillary information which describes the exterior orientation (i.e., look angle, attitude, and satellite position) and a 30 m SRTM DEM to correct for topographic distortions. The orthorectified and coregistered images were then correlated using COSI-Corr's phase correlator with a sliding window of 32 × 32 pixels and step of eight pixels, producing a disparity map of the horizontal surface displacement at 80 m resolution.

To measure fault-parallel and fault-perpendicular displacements, we first measured the offset across the fault in the north-south and east-west components (Figure S1 in Supporting Information S1; Table S4). We stacked 10-km-long profiles within a swath width (~0.8 km) to minimize the effect of noise. The uncertainty of the measurement is represented by a set of the minimum, optimal, and maximum values, which are obtained in association with the trend lines drawn on the data on both sides of the deformation zone (Figure S1 in Supporting Information S1). Horizontal slip vectors were then calculated by adding the north-south and east-west components of cross-fault displacements. We used the motion of the southern side of the rupture as the reference, that is, eastward (+) and southward (+). Then, we projected the composite horizontal slip vectors into fault-parallel and fault-perpendicular, using the strike of faults segment-wise.

We also measured the width of the deformation zone while measuring the east-west component in each swath profile (Figure S1 in Supporting Information S1 and Table S4). The fault-perpendicular width of offsets is a proxy for the extent of inelastic shear strain on either side of the primary, localized fault trace.

The off-fault deformation was calculated by subtracting the field observations (D1), which are assumed to capture the primary on-fault displacement, from the total displacement estimated by stacked profiles of optical correlation (D0). The ratio of off-fault deformation is thus defined as (D0-D1)/D0. In sections where field measurements are sparse or lacking, we drew an envelope of field measurements extrapolated from sides and estimated the off-fault deformation ratio using the envelope as a reference.

Appendix D: Estimation of Block Rotation Rate

Three approaches of estimation suggest a rotation rate of ~2°/Myr, which are generally consistent to each other. First, the rotation rate can be estimated in the framework of bookshelf model following the equations derived in Milliner et al. (2021); Platt and Becker (2013). If the regional right-lateral shear displacement (γ) and the angle between the conjugate and bounding faults (α) are known, then the amount of sinistral slip along the array of conjugate faults (γ') expected from bookshelf faulting and the rotation of block (ω) can be estimated from the following geometric relations:

$$\gamma' = \gamma \cdot \cos(2\alpha) \tag{D1}$$

$$\omega = \frac{\gamma}{2} \cdot (1 - \cos(2\alpha))/\mathrm{h} \tag{D2}$$

The clockwise rotation (ω) is coupled with the general N095°-striking left-lateral Kunlun and Ganze-Xianshuihe faults (γ'), to accommodate the broad right-lateral shearing in the ~N017°-trending India push relative to the

Sichuan basin (Bettinelli et al., 2006). From these geometric relations, $\gamma' = -10$ mm/yr (the slip rate of the Kunlun fault), and the average width of the block $h = \sim 300$ km, $\alpha = 78°$, and $\omega = 2.0°$/Myr.

The rotation rate can also be evaluated under the assumption of non-rigid bookshelf fault model for the Cenozoic tectonic development of north Tibet by Zuza and Yin (2016). First-order deformation in the block can be quantified as a continuous velocity field as a shear zone of a width h and the velocity across the shear zone (γ'). The rotation rate (ω) is defined as

$$\omega = \tan^{-1}\left(\frac{-\gamma'}{h}\right) \tag{D3}$$

For the Bayan Har block, $h = 300$ km and $\gamma' \sim 10$ mm/yr., the rotation rate (ω) is thus ~2°/Myr.

Third, England and Molnar (1990) hypothesized a large-scale north-striking simple shear model of the eastern Tibetan Plateau and predicted clockwise rotation of 1–2°/Myr of crustal block bounded by the east-striking left-lateral faults. Their estimation, which was based on the simplified assumption of NS-component right-lateral shear of 15–30 mm/yr over a zone of 1,000 km wide in EW-direction, captured the order-of-magnitude range before the age of dense GPS observations.

Conflict of Interest

The authors declare no conflicts of interest relevant to this study.

Data Availability Statement

All data presented in this manuscript are available in Supporting Information S1, including tables and figures for the purposes of peer review. Data will be eventually deposited and available on the Harvard Dataverse website (https://doi.org/10.7910/DVN/AQVRBV).

Acknowledgments

We thank colleagues from the Qinghai Bureau of CEA and the drone vendor for assistance in data acquisition; Mike Oskin, Liqing Jiao, Jin-Hyuck Choi, Shengji Wei, Han Yue, Xing Wang, Ken Hudnut, Paul Tapponnier, Chen Ji and Jihong Liu for helpful discussions; the editors and Yuri Fialko, John Fletcher and anonymous reviewers for their helpful comments and suggestions. This project was jointly supported by National Nonprofit Fundamental Research Grant of China, Institute of Geology, China Earthquake Administration (IGCEA1812), NSFC (42030305, 42202232, 42272242), the National Key Research and Development Program of China (2021YFC300605), and the State Key Laboratory of Earthquake Dynamic of China (LED2020B03).

References

Allen, C. R., Zhuoli, L., Hong, Q., Xueze, W., Huawei, Z., & Weishi, H. (1991). Field study of a highly active fault zone: The Xianshuihe fault of southwestern China. *GSA Bulletin*, *103*(9), 1178–1199. https://doi.org/10.1130/0016-7606(1991)103<1178:FSOAHA>2.3.CO;2

Antoine, S. L., Klinger, Y., Delorme, A., Wang, K., Bürgmann, R., & Gold, R. D. (2021). Diffuse deformation and surface faulting distribution from submetric image correlation along the 2019 Ridgecrest, California, ruptures. *Bulletin of the Seismological Society of America*, *111*(5), 2275–2302. https://doi.org/10.1785/0120210036

Antoine, S. L., Klinger, Y., Liu, Z., & Delorme, A. (2023). *Interplay between quasi-static and dynamic processes explains the surface deformation associated with the 2021 Mw 7.4 Maduo, Tibet, rupture* (pp. T31C–0219). AGU fall meeting.

Armijo, R., Meyer, B., Hubert, A. L., & Barka, A. (1999). Westward propagation of the North Anatolian fault into the northern Aegean: Timing and kinematics. *Geology*, *27*(3), 267–270. https://doi.org/10.1130/0091-7613(1999)027<0267:WPOTNA>2.3.CO;2

Avouac, J.-P., & Tapponnier, P. (1993). Kinematic model of active deformation in central Asia. *Geophysical Research Letters*, *20*(10), 895–898. https://doi.org/10.1029/93gl00128

Bao, X., Song, X., Eaton, D. W., Xu, Y., & Chen, H. (2020). Episodic lithospheric deformation in eastern Tibet inferred from seismic anisotropy. *Geophysical Research Letters*, *47*(3), e2019GL085721. https://doi.org/10.1029/2019GL085721

Bettinelli, P., Avouac, J.-P., Flouzat, M., Jouanne, F., Bollinger, L., Willis, P., & Chitrakar, G. R. (2006). Plate motion of India and interseismic strain in the Nepal Himalaya from GPS and DORIS measurements. *Journal of Geodesy*, *80*(8), 567–589. https://doi.org/10.1007/s00190-006-0030-3

Bruhat, L., Fang, Z., & Dunham, E. M. (2016). Rupture complexity and the supershear transition on rough faults. *Journal of Geophysical Research: Solid Earth*, *121*(1), 210–224. https://doi.org/10.1002/2015jb012512

Byerlee, J. (1978). Friction of rocks. *Pure and Applied Geophysics*, *116*(4), 615–626. https://doi.org/10.1007/BF00876528

Chen, K., Avouac, J.-P., Geng, J., Liang, C., Zhang, Z., Li, Z., & Zhang, S. (2022). The 2021 Mw 7.4 Madoi earthquake: An archetype bilateral slip-pulse rupture arrested at a splay fault. *Geophysical Research Letters*, *49*(2), e2021GL095243. https://doi.org/10.1029/2021GL095243

Cheng, C., Wang, D., Yao, Q., Fang, L., Xu, S., Huang, Z., et al. (2023). The 2021 Mw 7.3 Madoi, China earthquake: Transient supershear ruptures on a presumed immature strike-slip fault. *Journal of Geophysical Research: Solid Earth*, *128*(2), e2022JB024641. https://doi.org/10.1029/2022JB024641

Chester, F. M., & Chester, J. S. (2000). Stress and deformation along wavy frictional faults. *Journal of Geophysical Research*, *105*(B10), 23421–23430. https://doi.org/10.1029/2000jb900241

Cowie, P. A., & Scholz, C. H. (1992). Growth of faults by accumulation of seismic slip. *Journal of Geophysical Research*, *97*(B7), 11085–11095. https://doi.org/10.1029/92jb00586

Dolan, J. F., & Haravitch, B. D. (2014). How well do surface slip measurements track slip at depth in large strike-slip earthquakes? The importance of fault structural maturity in controlling on-fault slip versus off-fault surface deformation. *Earth and Planetary Science Letters*, *388*, 38–47. https://doi.org/10.1016/j.epsl.2013.11.043

Du, Y., & Aydin, A. (1995). Shear fracture patterns and connectivity at geometric complexities along strike-slip faults. *Journal of Geophysical Research*, *100*(B9), 18093–18102. https://doi.org/10.1029/95JB01574

Duan, B., & Day, S. M. (2008). Inelastic strain distribution and seismic radiation from rupture of a fault kink. *Journal of Geophysical Research*, *113*(B12), B12311. https://doi.org/10.1029/2008JB005847

Dunham, E. M., Belanger, D., Cong, L., & Kozdon, J. E. (2011). Earthquake ruptures with strongly rate-weakening friction and off-fault plasticity, part 2: Nonplanar Faults. *Bulletin of the Seismological Society of America*, *101*(5), 2308–2322. https://doi.org/10.1785/0120100076

England, P., & Molnar, P. (1990). Right-lateral shear and rotation as the explanation for strike-slip faulting in eastern Tibet. *Nature*, *344*(6262), 140–142. https://doi.org/10.1038/344140a0

Fialko, Y., & Jin, Z. (2021). Simple shear origin of the cross-faults ruptured in the 2019 Ridgecrest earthquake sequence. *Nature Geoscience*, *14*(7), 513–518. https://doi.org/10.1038/s41561-021-00758-5

Fletcher, J. M., Oskin, M. E., & Teran, O. J. (2016). The role of a keystone fault in triggering the complex El Mayor–Cucapah earthquake rupture. *Nature Geoscience*, *9*(4), 303–307. https://doi.org/10.1038/ngeo2660

Fletcher, J. M., Teran, O. J., Rockwell, T. K., Oskin, M. E., Hudnut, K. W., Spelz, R. M., et al. (2020). An analysis of the factors that control fault zone architecture and the importance of fault orientation relative to regional stress. *GSA Bulletin*, *132*(9–10), 2084–2104. https://doi.org/10.1130/B35308.1

Fu, B., & Awata, Y. (2007). Displacement and timing of left-lateral faulting in the Kunlun fault zone, northern Tibet, inferred from geologic and geomorphic features. *Journal of Asian Earth Sciences*, *29*(2), 253–265. https://doi.org/10.1016/j.jseaes.2006.03.004

Guo, H., Lay, T., & Brodsky, E. E. (2023). Seismological indicators of geologically inferred fault maturity. *Journal of Geophysical Research: Solid Earth*, *128*(10), e2023JB027096. https://doi.org/10.1029/2023JB027096

Hubbard, J., Barbot, S., Hill, E. M., & Tapponnier, P. (2015). Coseismic slip on shallow décollement megathrusts: Implications for seismic and tsunami hazard. *Earth-Science Reviews*, *141*, 45–55. https://doi.org/10.1016/j.earscirev.2014.11.003

Hudnut, K. W., Seeber, L., & Pacheco, J. (1989). Cross-fault triggering in the November 1987 Superstition Hills earthquake sequence, southern California. *Geophysical Research Letters*, *16*(2), 199–202. https://doi.org/10.1029/gl016i002p00199

Jin, Z., & Fialko, Y. (2021). Coseismic and early postseismic deformation due to the 2021 M7.4 Maduo (China) earthquake. *Geophysical Research Letters*, *48*(21), e2021GL095213. https://doi.org/10.1029/2021GL095213

Jin, Z., Fialko, Y., Yang, H., & Li, Y. (2023). Transient deformation excited by the 2021 M7.4 Maduo (China) earthquake: Evidence of a deep shear zone. *Journal of Geophysical Research: Solid Earth*, *128*(8), e2023JB026643. https://doi.org/10.1029/2023JB026643

Klinger, Y. (2010). Relation between continental strike-slip earthquake segmentation and thickness of the crust. *Journal of Geophysical Research*, *115*(B7), B07306. https://doi.org/10.1029/2009JB006550

Leprince, S., Ayoub, F., Klinger, Y., & Avouac, J. P. (2007). Co-Registration of Optically Sensed Images and Correlation (COSI-Corr): An operational methodology for ground deformation measurements. In *2007 IEEE international geoscience and remote sensing Symposium*.

Li, C., Li, T., Hollingsworth, J., Zhang, Y., Qian, L., & Shan, X. (2023). Strain threshold for the formation of coseismic surface rupture. *Geophysical Research Letters*, *50*(16), e2023GL103666. https://doi.org/10.1029/2023GL103666

Li, C., Li, T., Shan, X., & Zhang, G. (2023). Extremely large off-fault deformation during the 2021 Mw 7.4 Maduo, Tibetan plateau, earthquake. *Seismological Research Letters*, *94*(1), 39–51. https://doi.org/10.1785/0220220139

Lindsey, E. O., Fialko, Y., Bock, Y., Sandwell, D. T., & Bilham, R. (2014). Localized and distributed creep along the southern San Andreas fault. *Journal of Geophysical Research: Solid Earth*, *119*(10), 7909–7922. https://doi.org/10.1002/2014JB011275

Liu-Zeng, J., Liu, Z., Liu, X., Milliner, C., Padilla, A. M. R., Xu, S., et al. (2024). Replication data for: Fault orientation trumps fault maturity in controlling coseismic rupture characteristics of the 2021 Maduo earthquake [Dataset]. *Harvard Dataverse*. https://doi.org/10.7910/DVN/AQVRBV

Liu-Zeng, J., Yao, W., Liu, X., Shao, Y., Wang, W., Han, L., et al. (2022). High-resolution structure-from-motion models covering 160 km-long surface ruptures of the 2021 Mw 7.4 Madoi earthquake in northern Tibet. *Earthquake Research Advances*, *2*(2), 100140. https://doi.org/10.1016/j.eqrea.2022.100140

Manighetti, I., Campillo, M., Bouley, S., & Cotton, F. (2007). Earthquake scaling, fault segmentation, and structural maturity. *Earth and Planetary Science Letters*, *253*(3), 429–438. https://doi.org/10.1016/j.epsl.2006.11.004

Manighetti, I., Mercier, A., & De Barros, L. (2021). Fault trace corrugation and segmentation as a measure of fault structural maturity. *Geophysical Research Letters*, *48*(20), e2021GL095372. https://doi.org/10.1029/2021GL095372

Manighetti, I., Tapponnier, P., Courtillot, V., Gallet, Y., Jacques, E., & Gillot, P.-Y. (2001). Strain transfer between disconnected, propagating rifts in Afar. *Journal of Geophysical Research*, *106*(B7), 13613–13665. https://doi.org/10.1029/2000jb900454

Michel, R., & Avouac, J.-P. (2006). Coseismic surface deformation from air photos: The Kickapoo step over in the 1992 Landers rupture. *Journal of Geophysical Research*, *111*(B3), B03408. https://doi.org/10.1029/2005JB003776

Milliner, C., Donnellan, A., Aati, S., Avouac, J.-P., Zinke, R., Dolan, J. F., et al. (2021). Bookshelf kinematics and the effect of dilatation on fault zone inelastic deformation: Examples from optical image correlation measurements of the 2019 Ridgecrest earthquake sequence. *Journal of Geophysical Research: Solid Earth*, *126*(3), e2020JB020551. https://doi.org/10.1029/2020JB020551

Milliner, C. W. D., Dolan, J. F., Hollingsworth, J., Leprince, S., Ayoub, F., & Sammis, C. G. (2015). Quantifying near-field and off-fault deformation patterns of the 1992 Mw 7.3 Landers earthquake. *Geochemistry, Geophysics, Geosystems*, *16*(5), 1577–1598. https://doi.org/10.1002/2014gc005693

Mitchell, T. M., & Faulkner, D. R. (2009). The nature and origin of off-fault damage surrounding strike-slip fault zones with a wide range of displacements: A field study from the Atacama fault system, northern Chile. *Journal of Structural Geology*, *31*(8), 802–816. https://doi.org/10.1016/j.jsg.2009.05.002

Naylor, M. A., Mandl, G., & Supesteijn, C. H. K. (1986). Fault geometries in basement-induced wrench faulting under different initial stress states. *Journal of Structural Geology*, *8*(7), 737–752. https://doi.org/10.1016/0191-8141(86)90022-2

Pan, J., Li, H., Chevalier, M.-L., Tapponnier, P., Bai, M., Li, C., et al. (2022). Co-seismic rupture of the 2021, Mw7.4 Maduo earthquake (northern Tibet): Short-cutting of the Kunlun fault big bend. *Earth and Planetary Science Letters*, *594*, 117703. https://doi.org/10.1016/j.epsl.2022.117703

Perrin, C., Manighetti, I., Ampuero, J.-P., Cappa, F., & Gaudemer, Y. (2016). Location of largest earthquake slip and fast rupture controlled by along-strike change in fault structural maturity due to fault growth. *Journal of Geophysical Research: Solid Earth*, *121*(5), 3666–3685. https://doi.org/10.1002/2015jb012671

Perrin, C., Manighetti, I., & Gaudemer, Y. (2016). Off-fault tip splay networks: A genetic and generic property of faults indicative of their long-term propagation. *Comptes Rendus Geoscience*, *348*(1), 52–60. https://doi.org/10.1016/j.crte.2015.05.002

Perrin, C., Waldhauser, F., & Scholz, C. H. (2021). The shear deformation zone and the smoothing of faults with displacement. *Journal of Geophysical Research: Solid Earth*, *126*(5), e2020JB020447. https://doi.org/10.1029/2020JB020447

Petersen, M. D., Dawson, T. E., Chen, R., Cao, T., Wills, C. J., Schwartz, D. P., & Frankel, A. D. (2011). Fault displacement hazard for strike-slip faults. *Bulletin of the Seismological Society of America*, *101*(2), 805–825. https://doi.org/10.1785/0120100035

Platt, J. P., & Becker, T. W. (2013). Kinematics of rotating panels of E–W faults in the San Andreas system: What can we tell from geodesy? *Geophysical Journal International*, *194*(3), 1295–1301. https://doi.org/10.1093/gji/ggt189

Powers, P. M., & Jordan, T. H. (2010). Distribution of seismicity across strike-slip faults in California. *Journal of Geophysical Research*, *115*(B5), B05305. https://doi.org/10.1029/2008JB006234

Qinghai Institute of Geological Survey. (2010). Geologic map of the Maduo county (1:100,000 scale).

Ren, J., Xu, X., Zhang, G., Wang, Q., Zhang, Z., Gai, H., & Kang, W. (2022). Coseismic surface ruptures, slip distribution, and 3D seismogenic fault for the 2021 Mw 7.3 Maduo earthquake, central Tibetan Plateau, and its tectonic implications. *Tectonophysics*, *827*, 229275. https://doi.org/10.1016/j.tecto.2022.229275

Rodriguez Padilla, A. M., Oskin, M. E., Milliner, C. W. D., & Plesch, A. (2022). Accrual of widespread rock damage from the 2019 Ridgecrest earthquakes. *Nature Geoscience*, *15*(3), 222–226. https://doi.org/10.1038/s41561-021-00888-w

Roger, F., Jolivet, M., & Malavieille, J. (2010). The tectonic evolution of the Songpan-Garzê (north Tibet) and adjacent areas from Proterozoic to present: A synthesis. *Journal of Asian Earth Sciences*, *39*(4), 254–269. https://doi.org/10.1016/j.jseaes.2010.03.008

Ron, H., Beroza, G., & Nur, A. (2001). Simple model explains complex faulting. *Eos, Transactions American Geophysical Union*, *82*(10), 125–129. https://doi.org/10.1029/eo082i010p00125-01

Sarmiento, A., Madugo, D., Bozorgnia, Y., Shen, A., Mazzoni, S., Lavrentiadis, G., et al. (2021). Report GIRS 2021-08: Fault displacement hazard initiative database. Retrieved from https://www.risksciences.ucla.edu/girs-reports/2021/08

Scholz, C. H., Ando, R., & Shaw, B. E. (2010). The mechanics of first order splay faulting: The strike-slip case. *Journal of Structural Geology*, *32*(1), 118–126. https://doi.org/10.1016/j.jsg.2009.10.007

Sibson, R., Ghisetti, F., & Ristau, J. (2011). Stress control of an evolving strike-slip fault system during the 2010–2011 Canterbury, New Zealand, earthquake sequence. *Seismological Research Letters*, *82*(6), 824–832. https://doi.org/10.1785/gssrl.82.6.824

Sibson, R. H. (1990). Rupture nucleation on unfavorably oriented faults. *Bulletin of the Seismological Society of America*, *80*(6A), 1580–1604. https://doi.org/10.1785/BSSA08006A1580

Sieh, K., Jones, L., Hauksson, E., Hudnut, K., Eberhart-Phillips, D., Heaton, T., et al. (1993). Near-field investigations of the Landers earthquake sequence, April to July 1992. *Science*, *260*(5105), 171–176. https://doi.org/10.1126/science.260.5105.171

Stirling, M. W., Wesnousky, S. G., & Shimazaki, K. (1996). Fault trace complexity, cumulative slip, and the shape of the magnitude-frequency distribution for strike-slip faults: A global survey. *Geophysical Journal International*, *124*(3), 833–868. https://doi.org/10.1111/j.1365-246x.1996.tb05641.x

Sylvester, A. G. (1988). Strike-slip faults. *Geological Society of America Bulletin*, *100*(11), 1666–1703. https://doi.org/10.1130/0016-7606(1988)100<1666:SSF>2.3.CO;2

Tapponnier, P., Xu, Z., Roger, F., Meyer, B., Arnaud, N., Wittlinger, G., & Yang, J. (2001). Oblique stepwise Rise and growth of the Tibet Plateau. *Science*, *294*(5547), 1671–1677. https://doi.org/10.1126/science.105978

Tchalenko, J. S. (1970). Similarities between shear zones of different magnitudes. *GSA Bulletin*, *81*(6), 1625–1640. https://doi.org/10.1130/0016-7606(1970)81[1625:SBSZOD]2.0.CO;2

Templeton, E. L., & Rice, J. R. (2008). Off-fault plasticity and earthquake rupture dynamics: 1. Dry materials or neglect of fluid pressure changes. *Journal of Geophysical Research*, *113*(B9), B09306. https://doi.org/10.1029/2007JB005529

Teran, O. J., Fletcher, J. M., Oskin, M. E., Rockwell, T. K., Hudnut, K. W., Spelz, R. M., et al. (2015). Geologic and structural controls on rupture zone fabric: A field-based study of the 2010 Mw 7.2 El Mayor–Cucapah earthquake surface rupture. *Geosphere*, *11*(3), 899–920. https://doi.org/10.1130/GES01078.1

Thatcher, W., & Hill, D. P. (1991). Fault orientations in extensional and conjugate strike-slip environments and their implications. *Geology*, *19*(11), 1116–1120. https://doi.org/10.1130/0091-7613(1991)019<1116:FOIEAC>2.3.CO;2

Thomas, M. Y., & Bhat, H. S. (2018). Dynamic evolution of off-fault medium during an earthquake: A micromechanics based model. *Geophysical Journal International*, *214*(2), 1267–1280. https://doi.org/10.1093/gji/ggy129

Vallage, A., Klinger, Y., Grandin, R., Bhat, H. S., & Pierrot-Deseilligny, M. (2015). Inelastic surface deformation during the 2013 Mw 7.7 Balochistan, Pakistan, earthquake. *Geology*, *43*(12), 1079–1082. https://doi.org/10.1130/G37290.1

Van der Woerd, J., Ryerson, F. J., Tapponnier, P., Meriaux, A.-S., Gaudemer, Y., Meyer, B., et al. (2000). Uniform slip-rate along the Kunlun fault: Implications for seismic behaviour and large-scale tectonics. *Geophysical Research Letters*, *27*(16), 2353–2356. https://doi.org/10.1029/1999gl011292

Wang, E. (1998). *Late Cenozoic Xianshuihe-Xiaojiang, Red River, and Dali fault systems of southwestern Sichuan and central Yunnan, China* (Vol. 327). Geological Society of America.

Wang, M., & Shen, Z.-K. (2020). Present-day crustal deformation of continental China derived from GPS and its tectonic implications. *Journal of Geophysical Research: Solid Earth*, *125*(2), e2019JB018774. https://doi.org/10.1029/2019JB018774

Wang, W., Fang, L., Wu, J., Tu, H., Chen, L., Lai, G., & Zhang, L. (2021). Aftershock sequence relocation of the 2021 Ms7.4 Maduo earthquake, Qinghai, China. *Science China Earth Sciences*, *51*(07), 1193–1202. https://kns.cnki.net/kcms/detail/11.5842.P.20210618.1049.002.html

Wei, S., Zeng, H., Shi, Q., Liu, J., Luo, H., Hu, W., et al. (2022). Simultaneous rupture propagation through fault bifurcation of the 2021 Mw7.4 Maduo earthquake. *Geophysical Research Letters*, *49*(21), e2022GL100283. https://doi.org/10.1029/2022GL100283

Wells, D. L., & Coppersmith, K. J. (1994). New empirical relationships among magnitude, rupture length, rupture width, rupture area, and surface displacement. *Bulletin of the Seismological Society of America*, *84*(4), 974–1002. https://doi.org/10.1785/BSSA0840040974

Wesnousky, S. G. (1988). Seismological and structural evolution of strike-slip faults. *Nature*, *335*(6188), 340–343. https://doi.org/10.1038/335340a0

Wilcox, R. E., Harding, T. P., & Seely, D. R. (1973). Basic Wrench Tectonics1. *AAPG Bulletin*, *57*(1), 74–96. https://doi.org/10.1306/819A424A-16C5-11D7-8645000102C1865D

Xie, F.-R., Chen, Q.-C., Cui, X.-F., Li, H., Yang, S., Guo, Q., et al. (2007). Fundamental database of crustal stress environment in continental China. *Progress in Geophysics*, *22*(1), 131–136.

Xu, S., Fukuyama, E., Ben-Zion, Y., & Ampuero, J.-P. (2015). Dynamic rupture activation of backthrust fault branching. *Tectonophysics*, *644–645*, 161–183. https://doi.org/10.1016/j.tecto.2015.01.011

Yuan, Z., Li, T., Su, P., Sun, H., Ha, G., Guo, P., et al. (2022). Large surface-rupture gaps and low surface fault slip of the 2021 Mw 7.4 Maduo earthquake along a low-activity strike-slip fault, Tibetan Plateau. *Geophysical Research Letters*, *49*(6), e2021GL096874. https://doi.org/10.1029/2021GL096874

Yue, H., Shen, Z.-K., Zhao, Z., Wang, T., Cao, B., Li, Z., et al. (2022). Rupture process of the 2021 M7.4 Maduo earthquake and implication for deformation mode of the Songpan-Ganzi terrane in Tibetan Plateau. *Proceedings of the National Academy of Sciences*, *119*(23), e2116445119. https://doi.org/10.1073/pnas.2116445119

Zhang, J., Wang, X., Chen, L., & Liu, J. (2022). Seismotectonics and fault geometries of the Qinghai Madoi Ms 7.4 earthquake sequence: Insight from aftershock relocations and focal mechanism solutions. *Chinese Journal of Geophysics*, *65*(2), 552–562. https://doi.org/10.6038/cjg2022P0516

Zhu, Y., Diao, F., Fu, Y., Liu, C., & Xiong, X. (2021). Slip rate of the seismogenic fault of the 2021 Maduo earthquake in Western China inferred from GPS observations. *Science China Earth Sciences*, *64*(8), 1363–1370. https://doi.org/10.1007/s11430-021-9808-0

Zuza, A. V., & Yin, A. (2016). Continental deformation accommodated by non-rigid passive bookshelf faulting: An example from the Cenozoic tectonic development of northern Tibet. *Tectonophysics*, *677–678*, 227–240. https://doi.org/10.1016/j.tecto.2016.04.007